

# Electron contamination modeling and reduction in a 1 T open bore inline MRI-Linac system

B. M. Oborn<sup>1,2</sup>, S. Kolling<sup>3</sup>, P. E. Metcalfe<sup>2,6</sup>, S. Crozier<sup>4</sup>, D. W. Litzenberg<sup>5</sup>, P. J. Keall<sup>3,6</sup>.

<sup>1</sup>Illawarra Cancer Care Centre (ICCC), Wollongong, NSW 2500, Australia.

<sup>2</sup>Centre for Medical Radiation Physics (CMRP), University of Wollongong, Wollongong, NSW 2500, Australia.

<sup>3</sup>Sydney Medical School, University of Sydney, NSW 2006, Australia.

<sup>4</sup>School of Information Technology and Electric Engineering, University of Queensland, QLD 4072, Australia.

<sup>5</sup>Department of Radiation Oncology, University of Michigan Hospital and Health Systems, Ann Arbor, MI 48109, USA

<sup>6</sup>Ingham Institute for Applied Medical Research, Liverpool, NSW, 2170, Australia.

## Abstract

**Purpose:** A potential side effect of inline MRI-Linac systems is electron contamination focusing causing a high skin dose. In this work we reexamine this prediction for an open bore 1 T MRI system being constructed for the Australian MRI-Linac Program. The efficiency of an electron contamination deflector (ECD) in purging electron contamination from the linac head is modeled, as well as the impact of a helium gas region between the deflector and phantom surface for lowering the amount of air-generated contamination.

**Methods:** Magnetic modeling of the 1 T MRI was used to generate 3D magnetic field maps both with and without the presence of an ECD located immediately below the MLC's. 47 different ECD designs were modeled and for each the magnetic field map was imported into Geant4 Monte Carlo simulations including the Linac head, ECD, and a 30x30x30 cm<sup>3</sup> water phantom located at isocentre. For our first generation system the x-ray source to isocentre distance (SID) will be 160 cm, resulting in an 81.2 cm long air gap from the base of the ECD to the phantom surface. The first 71.2 cm was modeled as air or helium gas, with the latter encased between two windows of 50  $\mu$ m thick high density polyethylene. 2D skin doses (at 70  $\mu$ m depth) were calculated across the phantom surface at 1x1 mm<sup>2</sup> resolution for 6MV beams of field size of 5x5, 10x10 and 20x20 cm<sup>2</sup>.

**Results:** The skin dose was predicted to be of similar magnitude as the generic systems modeled in previous work, 230% to 1400% of  $D_{max}$  for 5x5 to 20x20 cm<sup>2</sup> respectively.

Inclusion of the ECD introduced a non-uniformity to the MRI imaging field that ranged from  $\sim$ 20 to  $\sim$ 140 ppm while the net force acting on the ECD ranged from  $\sim$ 151 N to  $\sim$ 1773 N. Various ECD designs were 100% efficient at purging the electron contamination into the ECD magnet banks, however a small percentage were scattered back into the beam and continued to the phantom surface. Replacing a large portion of the extended air-column between the ECD and phantom surface with helium gas is a key element as it significantly minimised the air-generated contamination.

When using an optimal ECD and helium gas region, the 70  $\mu$ m skin dose is predicted to increase moderately inside a small hot spot over that of the case with no magnetic field present for the jaw defined square beams examined here. These increases include from 12% to 40% of  $D_{max}$  for 5x5 cm<sup>2</sup>, 18% to 55% of  $D_{max}$  for 10x10 cm<sup>2</sup>, and from 23% to 65% of  $D_{max}$  for 20x20 cm<sup>2</sup>.

**Conclusions:** Including an optimised ECD and helium gas region below the MLCs in our 160 cm isocentre MRI-linac system is predicted to ameliorate the impact electron contamination focusing has on skin dose increases. An ECD is practical as its impact on the MRI imaging distortion is correctable, and the mechanical forces acting on it manageable from an engineering point of view.

Key words: MRI-linac, electron contamination, skin dose, Monte Carlo simulation, magnetic deflector

## I. INTRODUCTION

MRI-guided radiotherapy as delivered by an MRI-linac (MRL), is showing promise as potentially a major advance in cancer radiotherapy. Firstly, the modality will offer real time MR-quality images of the patient anatomy. Secondly,

45 when coupled with the dynamic real time operation of a multileaf collimator (MLC) modulated radiotherapy beam,  
46 there is the expectation that moving tumors can be treated with the tightest margins. The end result would be a  
47 reduction in dose to healthy tissue - lower toxicity, while at the same time dose escalation to the tumor - higher local  
48 control rates. In essence this is a more ideal radiotherapy treatment.

49 At present the group from UMC Utrecht have a second generation MRI-linac system consisting of a Philips 1.5  
50 T closed bore MRI and an Elekta 6MV linac[1]. At the Cross Cancer Institute a bi-directional linac-MR system  
51 consisting of a Varian linac (6MV) and a 0.56 T MRI system[2] is being built. Although technically not an MRI-linac,  
52 the ViewRay[3] system is a related device comprised of three Cobalt-60 radiation sources within a 0.35 T MRI scanner.  
53 Finally, as elaborated in this work, a 1 T open bore MRI-linac system is under development at the Ingham Research  
54 Institute, Sydney Australia. This system will utilize a Varian based 6MV x-ray beam and 120 leaf MLC, and a custom  
55 designed 1 T open bore MRI system built by Agilent Technologies, Oxford, United Kindom.

56 This particular open bore design was first envisaged in the related 2011 work by Constantin et al[4]. In that work  
57 a 0.5 T GE Signa split bore MRI system was modeled for its impact on electron guns operating inside the fringe field  
58 of the MRI.

59 The Sydney system is similarly designed to operate without any magnetic shielding of the linac head. The MRI field  
60 has been specially designed to include low magnetic field regions ( $\sim 0$  T) where the linac x-ray target and waveguide  
61 will lie. Further to this, the generation I system will not rotate the linac - instead a rotating couch is planned.

62 For the purposes of this work we will define an open bore MRI system as one which has the magnetic field source  
63 coils separated into two halves such that a patient could be placed through or between the gap. Thus a patient could  
64 be exposed to a radiation beam that travels down the bore and is parallel or inline with the MR imaging field at the  
65 isocentre: inline MRIgRT. This type of system however still inherently allows a patient to be placed inside the bore  
66 and a radiation beam travel through the gap perpendicular to the magnetic field direction: perpendicular MRIgRT.  
67 Both the Alberta and the Sydney designs are therefore open bore designs, and are both planned for testing in the  
68 inline and perpendicular orientations.

69 Some drawbacks for MRI-guided radiotherapy include firstly the complexity of the engineering feat required to  
70 make an MRI-linac system operate as intended, and secondly accounting for the x-ray dose deposition changes induced  
71 by the magnetic field of the MRI scanner. A third drawback that is arguably not fully realized at this point in time  
72 is that of the quality assurance or dose delivery confirmation of such a system.

73 In terms of skin dose changes several studies have focused on this in both the perpendicular and inline orientations  
74 [5, 6, 7, 8, 9]. Of particular interest are the recent simulations performed by our group which predicted that the fringe  
75 field from an inline 1 T MRI-Linac system could act to focus electron contamination from the Linac head, resulting  
76 in large skin dose increases at the patient/phantom surface[7]. The focusing of electron contamination from a linac  
77 generated x-ray beam in a parallel magnetic field has been most notably first experimentally reported more than a  
78 decade ago[10], and later confirmed to match with simulations of the same arrangement[11]. In that work a 20 cm bore  
79 superconducting solenoid magnet was used to generate a strong magnetic field parallel to a 10 MV photon beam with a  
80 distance from the x-ray source to magnet centre of 250 cm. Film measurements showed a large but not quantitatively  
81 evaluated increase in the beam entry side surface dose. This film data has now been reprocessed in this current work  
82 to ascertain the magnitude, see section IIIA.

83 A technique used to lower the production of air-generated contamination in the extended air-column of the Litzen-  
84 berg experiment was replacement of the air with helium gas. This is a well known method being described as early as  
85 1979 [12]. This has been experimentally proven in various works since 1979 [13, 14, 15, 16, 17, 18]. Removal or purging  
86 of electron contamination from radiotherapy x-ray beams via some type of permanent or electromagnet system has

87 also a long and mostly successful history [19, 20, 21, 22, 23, 14, 24, 25, 26, 27, 15, 28, 17, 18].

88 The aim of this work is to reinvestigate our previous modeling predictions of high skin dose by accurately modeling  
89 the 1 T open bore MRI design which is now under construction. We also report on the use of a permanent magnet  
90 electron contamination deflector (ECD) system, located below the MLCs, to purge electron contamination arising  
91 from the linac head and collimation system. Finally, we aim to investigate the impact of replacing a large portion  
92 of the air column between the ECD and phantom surface with helium gas as a method of minimizing the amount of  
93 air-generated electron contamination that will otherwise transport directly to the phantom surface due to the strong  
94 parallel magnetic field of the MRI.

95 In this current simulation work, we have additional constraints on the properties of the electron contamination  
96 deflector. These constraints include the ability to generate a transverse magnetic field strong enough to deflect  
97 contamination whilst being subject to the background MRI fringe field, and secondly minimize the impact on the MR  
98 imaging uniformity. In order to have confidence in answering these questions, full Monte Carlo simulations of the linac  
99 head are performed which utilize accurate magnetic field maps taken from finite element modeling of the actual MRI  
100 and electron contamination deflector designs.

## 101 II. MATERIALS AND METHODS

### 103 II. A. Benchmark magnetic modeling of the MRI design

104 COMSOL Multiphysics[29] was used to set up a finite element model of the 1 T open bore MRI system which is  
105 currently under construction. The coil currents and configurations were modeled as provided by the manufacturer  
106 Agilent. In the first benchmarking simulations no ferromagnetic objects were included and the goal was to match the  
107 Agilent specifications, namely the properties of the imaging field and fringe field. In the imaging field, or the diameter  
108 of spherical volume (DSV) the most important quantity is the uniformity of the magnetic field in the z-direction,  $B_z$ .  
109 This uniformity is  $\pm 0.5$  ppm (20 cm DSV) and  $\pm 5$  ppm (30 cm DSV). A key design feature of the fringe field is low  
110 strength regions in both the inline and perpendicular systems where the linac will reside.

111 The boundary condition  $\vec{n} \cdot \vec{B} = 0$  was set at the boundary of the largest cylinder to encompass a finite size to  
112 the simulated volume. In the final model there were  $14 \times 10^6$  mesh elements, with around 90% of these inside an air  
113 volume of 6 m x 6 m (length x diameter) symmetric cylinder surrounding the coils.

114 Mesh size independence of the model was confirmed by a converging result with increasing resolution of the mesh  
115 size. This process is described in detail in recent work by our group[30].

116 The solver used was the stationary solver FGMRES, and the coils were described as External Current Density  
117 sources under the magnetic fields interface identifier which is part of the AC/DC physics module of COMSOL. In  
118 this benchmarking work a full 3D model was employed, similar to the non-symmetric models which included the ECD  
119 (next section). When solved the simulation took around 240 CPUh on 2.6 GHz AMD processors. The RAM required  
120 was around 200 GB.

### 122 II.B. Electron Contamination Deflector (ECD) magnetic modeling

123 A permanent magnet style electron contamination deflector system located below the MLC's was next included in  
124 the COMSOL simulations. This consisted of 2 banks of NdFeB (grade N38) rare-earth magnets with a plain carbon  
125 steel grade 1010 magnetic circuit to encourage flux to cross the magnet gap (see figure 1). The B-H curve of this  
126 material was sourced from the material library of the Ansys Maxwell3D software (Canonsburg, PA). The device was

127 modeled with a fixed gap to allow a maximum field size of  $20 \times 20 \text{ cm}^2$  to pass through without interference. The  
128 magnet bank thickness, steel thickness and magnet depth were varied. The values investigated were magnet bank  
129 thickness: 2 cm, 3 cm, 4 cm and 5 cm; steel thickness: 0.5 cm, 1 cm, 1.5 cm, 2.0 cm and 2.5 cm; ECD depth: 4 cm, 6  
130 cm and 8 cm. This resulted in the least massive design having 0.64 kg of NdFeB and 0.736 kg of steel 1010, and the  
131 most massive model having 6.4 kg of NdFeB and 5.44 kg of steel 1010. The impact of the ECD on the 30 cm diameter  
132 DSV uniformity was calculated for each combination.

133 Inside COMSOL the ECD steel was modeled as a case of Amperes' Law using the steel grade 1010 magnetisation  
134 (BH) curve under the magnetic fields interface identifier (AC/DC physics module) while the permanent magnets  
135 were also set up as a case of Amperes' Law with a remanent flux density of 1.3 T and relative permeability of 1.05  
136 as per the specifications of N38 grade NdFeB permanent magnets. For each simulation a Force Calculation node was  
137 included to calculate the net force acting on the ECD as a whole unit.

138 Meshing of this model included dedicated air volumes surrounding just the ECD. This improved mesh generation  
139 and minimised RAM requirements as much as possible while preserving the desired accuracy. When solved the  
140 simulations including the ECD designs took around 720 CPUh on 2.6 GHz AMD processors. The RAM required was  
141 around 220 GB.

142

## 143 *II.C. Monte Carlo simulations*

144 The Monte Carlo simulations were performed using Geant4.9.6.p01[31]. The physics processes used were the  
145 Livermore models and for electron stepping inside a magnetic field the 4th-order Runge-Kutter stepper was used.  
146 This stepping algorithm has been successfully benchmarked in the work by Raaijmakers et al[32]. The beam modeled  
147 was a 6 MV (Varian 2100C) photon beam[33]. The accuracy of this linac head model has been confirmed in previous  
148 work[5] for the Geant version 4.9.1. The same benchmarking measurements were repeated with version 4.9.6p02 and  
149 results were essentially identical. For all simulations, a phase space file was used as the input particles. The phase  
150 space was located at a plane at the base of the flattening filter. In the simulation which produced the phase space file,  
151 there was no magnetic field present. This has no impact on electron contamination properties as all contamination  
152 above the flattening filter is stopped by the filter itself, or the surrounding carousel base. The choice of generating the  
153 phase space without the presence of the MRI fringe field was made so that this data would reflect the most generic  
154 case, or a fully magnetically shielded region of the linac head. At this point in time it is unclear if such shielding  
155 will be required. As a quantitative measure of the impact of this approximation we also generated photon energy  
156 fluence maps of the phase space file which firstly included the fringe field and secondly for a  $\pm 10 \%$  change in the  
157 electron beam FWHM cross sectional size striking the x-ray target. Both changes had insignificant differences in the  
158 energy fluence maps. In other words the small fringe field had no significant impact on changing the resultant photon  
159 beam properties and hence phantom dose, and so the absence of the fringe magnetic field above the flattening filter is  
160 acceptable for this configuration simulated at 160 cm SID.

161 The simulation phantom consisted of a  $30 \times 30 \times 30 \text{ cm}^3$  water block positioned at isocentre. Thus the phantom  
162 surface was at 145 cm from the x-ray source. Scoring was performed in the entire phantom at a resolution of  $1 \text{ mm}^3$ ,  
163 as well as at higher depth resolution in the first 1 mm depth. The surface resolution was in  $10 \mu\text{m}$  thick layers in  
164 the first 0.1 mm and 0.1 mm thick layers from 0.1 mm to 1 mm depth. The 2D skin dose (at  $70 \mu\text{m}$  effective depth)  
165 was calculated as the average of the dose in the  $60\text{-}70 \mu\text{m}$  and  $70\text{-}80 \mu\text{m}$  layers across the phantom surface. This is  
166 designed to match the definition of the effective skin dose depth as described in the ICRP Report 59[34].

167 As a method to observe the path of electron contamination, the raw energy deposited per primary particle history  
168 in the phantom, helium or air column, and linac head was extracted inside each simulation. The scoring grid resolution

169 was  $2 \text{ mm}^3$  and extended over a  $30 \times 30 \times 150 \text{ cm}^3$  volume (from isocentre to 150 cm above isocentre).

170 The ECD was implemented in the Monte Carlo environment with the same geometry and materials as the corre-  
171 sponding COMSOL model simulation. The only addition to the design was a 5 mm thick high density polyethylene  
172 (HDPE) layer across the magnet and steel surfaces which faced the x-ray beam CAX direction. The HDPE cover  
173 was included in an effort to reduce backscattering of any deflected electrons which strike the magnet faces or steel.  
174 Without this there is an increased chance that these backscatter back into the beam path and become forced to travel  
175 towards the phantom surface.

176 The Monte Carlo particle step and cutoff parameters were set to  $5 \mu\text{m}$  in the first 1 mm of the phantom (surface  
177 dose layers) and 0.2 mm in all other volumes. Selection of these step and cutoff parameters ensures that electrons are  
178 tracked correctly in air and under the influence of magnetic fields. Typically  $6.5 \times 10^{11}$  or greater primary particle  
179 histories were simulated to achieve less than  $\pm 1\%$  statistical error in the voxels located at  $D_{\text{max}}$  in the phantom  
180 at  $1 \times 1 \times 1 \text{ mm}^3$  resolution. The time taken for each different simulation was around 480 CPUh on 2.6 GHz AMD  
181 processors. This resulted in error estimates of  $\pm 10\%$  in the skin dose region voxels of  $10 \mu\text{m}$  thick.

182

## 183 *II.D. Helium Gas Region*

184 The helium gas region was implemented in the Monte Carlo simulations by replacing the top 71.2 cm portion of  
185 the 81.2 cm air column between the ECD and phantom surface with helium gas. The final 10 cm air-gap between the  
186 helium region and phantom surface is deliberate and represents the extremity of the patient treatment volume where  
187 it would be impractical to place a helium gas region. It also corresponds to the lower edge of the cryostat wall and  
188 so is a practical location for termination of the helium region. To encase the helium gas a simple HDPE bag would  
189 be employed. This has been modelled as a  $50 \mu\text{m}$  thick layer at the top and bottom of the helium gas region. This  
190 layer in fact acts as a source of secondary electron scatter and having its thickness as thin as practically possible is  
191 desirable.

## 192 **III. RESULTS AND DISCUSSION**

### 193 **III.A. Reprocessed results from the 2001 Litzenberg experiments**

194 Figure 2 shows some selected and reprocessed film data from the 2001 Litzenberg experiments. In the main figure  
195 body, central axis depth-dose profiles are presented for the films exposed to magnetic fields of  $B = 0 \text{ T}$ ,  $B = 0.5 \text{ T}$ ,  
196 and  $B = 3 \text{ T}$ . Insert part (a) shows a zoomed plot of the first 3.5 cm depth while parts (b) and (c) show the 0 T and 3  
197 T films which the plots were extracted from. There is a strong increase in the surface dose, particularly at 3 T. This  
198 is a direct product of the fringe field from the magnet acting to collect and focus air-generated contamination along  
199 the beam CAX, with the majority being near the magnet cryostat edge. The 3 T result also shows that the surface  
200 dose starts at  $\sim 600\%$  and increases to  $\sim 1245\%$  at  $\sim 2.5 \text{ mm}$  depth. This is opposed to the 0.5 T film showing a  
201 maximum dose of almost 270% at the surface. It is expected that this is either due to when exposed, the 3 T film  
202 was protruding slightly from the phantom in which it was positioned inside, or the electron contamination spectrum  
203 incident upon the surface to have a higher average energy than the 0.5 T case. In the former theory lateral scatter  
204 from the thin film would prevent the film from showing the maximum dose at the surface, while in the latter a larger  
205 build-up effect would be seen relative to the 0.5 T case. Either way it is clear evidence that a high surface dose due  
206 to contamination focusing is a real effect, and its magnitude can easily exceed the dose at  $D_{\text{max}}$ .

### 207 **III.B. Benchmark magnetic modeling of the MRI design**

208 Figure 3 shows a magnetic field magnitude ( $|\vec{B}|$ ) plot through the magnet center for the 1 T MRI system as  
 209 calculated by the manufacturer. Overlaid on this image is a contour line plot from our COMSOL simulations showing  
 210 some of the magnetic field magnitude values. Two low field regions are also clearly identified and will be where the  
 211 linac will reside in either the inline or perpendicular configurations. In this plot the color white is shown in regions  
 212 above 2 T or below 0.06 T. An excellent match is seen between the contour and fill plots at the selected values of 0.06  
 213 T, 0.65, and 2 T. For a 30 cm DSV we obtain a 6.8 ppm spread, or  $\leq \pm 5$  ppm. This matches the manufacturer's  
 214 specifications of 1 T  $\pm 5$  ppm for a 30 cm DSV to within 4 decimal places. It is clear from figure 3 that an accurate  
 215 model of our MRI system has been developed inside COMSOL which matches the manufacturer's specifications. This  
 216 now gives us the ability to model the impact of a ferromagnetic ECD as described in section III.C.

### 217 III.C. Skin Dose without an Electron Contamination Deflector and helium gas region

218 To investigate the effect of SID variation on MRI-linac skin dose figure 4 displays some key results from the Monte  
 219 Carlo modeling. In each part the field size shown is 20x20 cm<sup>2</sup> at isocentre while the SID is varied from 100 cm to  
 220 130 cm and 160 cm.

221 In the top row is displayed the energy deposition along a central x-z slice (log-scale) throughout the linac head,  
 222 air column and phantom region. Superimposed on this is the magnetic field line directions (note figure 4(a) is  
 223 without magnetic field). In the middle row the 2D skin dose at 70  $\mu$ m depth is presented and in the bottom row the  
 224 corresponding x/y profiles at 70  $\mu$ m depth are compared with an average x/y profile at 15 mm depth.

225 In figure 4(a) the reference case of SID = 100 cm, and no magnetic field is shown. As expected the skin dose is  
 226 around 23% for the 20x20 cm<sup>2</sup> field, and along the beam CAX there is a gradual drop-off in the energy deposition  
 227 from the base of the flattening filter to the phantom level. This corresponds to electron contamination on average  
 228 scattering away from the beam CAX. In figure 4(b) the MRI field is introduced and the impact on the contamination is  
 229 immediately seen. Essentially contamination or in fact any scattered electron is trapped and encouraged to travel with  
 230 the MRI field lines. Instead of spreading over a large area they are contained. Further to this, all forward scattered  
 231 (towards isocentre) electrons produced by the flattening filter and ion chamber are collected and focused, rather than  
 232 diverging away from CAX. Here with the 20x20 cm<sup>2</sup> field we see the largest skin dose increase being around 29 times  
 233 that of the dose at 1.5 cm depth, or  $D_{\max}$  with a magnetic field at SID = 100 cm ( $29 \times D_{\max}$  for 10x10 cm<sup>2</sup>,  $24$   
 234  $\times D_{\max}$  for 5x5 cm<sup>2</sup>). The fact that the skin dose is the same for 20x20 cm<sup>2</sup> and 10x10 cm<sup>2</sup> is evidence that this  
 235 contamination arises mostly from the ion chamber and flattening filter. At 5x5 cm<sup>2</sup> there is a mild reduction as the  
 236 jaws partially block some contamination.

237 As we go to SID = 130 cm (figure 4(c)), the same processes are acting, however there is an overall stronger focusing  
 238 effect, resulting in a smaller cross-section for where all the contamination will enter the phantom. On the other hand  
 239 the jaws are closed more to account for the extended SID, in effect blocking some contamination. This overall leads  
 240 to even higher relative skin dose increases, in the order of 40 times that of the dose at  $D_{\max}$  for B = 0 T and 20x20  
 241 cm<sup>2</sup> field ( $29 \times D_{\max}$  for 10x10 cm<sup>2</sup>,  $8 \times D_{\max}$  for 5x5 cm<sup>2</sup>). This is higher than the SID = 100 cm case mostly due  
 242 to the reduction in cross-sectional area of the hot-spot.

243 Finally when we get to SID = 160 cm (figure 4(d)), there is a significant drop back to around 14 times the  $D_{\max}$   
 244 dose ( $5.5 \times D_{\max}$  for 10x10 cm<sup>2</sup>,  $2.5 \times D_{\max}$  for 5x5 cm<sup>2</sup>). This is attributed to both a natural purging of a portion  
 245 of the contamination above the jaws, as well as the further closing of the jaws to account for SID = 160 cm. There is  
 246 still a strong focusing of contamination below this level, as well as some propagation of electrons from the base of the  
 247 flattening filter and ion chamber, particularly those generated near CAX.

248 In contrast to the high skin doses presented in this work, recent modeling work performed by the Alberta group on  
 249 the skin/entry dose (average of the first 70  $\mu$ m dose) increases for their prototype 126 cm SID, 0.56 T inline MRI-linac

250 system was reported to be minor[8]. For that system the fringe field penetrating the linac head was modeled as  
251 insignificant and so they expect no contamination generated by the linac head to be collected and propagated towards  
252 the phantom. Only minor skin dose increases modeled were attributed to the final portion of the air column above  
253 the phantom having the same effect we see with contamination being transported directly to the phantom surface in  
254 the presence of the parallel magnetic field.

### 255 **III.D. Electron Contamination Deflector Modeling**

#### 256 **Impact on the MRI imaging field**

257 The inclusion of the various different ECD models had a direct impact on the 30 cm DSV uniformity ranging from  
258 20 ppm up to 140 ppm (see figure 5). As expected the designs with the greatest mass of steel frame generated the  
259 largest non-uniformities. The total mass of the magnetic material had far less impact than the steel, primarily because  
260 the relative permeability of the magnet material is constant at 1.05 whereas the steel is ferromagnetic and has a strong  
261 BH-curve response in B-fields, especially below 0.5 T where the ECD lies. In figure 6(a) we see a plot of the magnetic  
262 field magnitude in the linac region without (left side) and with (right side) the heaviest ECD. For this ECD design  
263 the magnet depth was 8 cm, the magnet thickness 5 cm, and the steel thickness 2.5 cm. This particular design has a  
264 30 cm DSV distortion of 140 ppm which is well below the 300 ppm threshold for correction via passive shimming as  
265 indicated in previous work[35]. From figure 6(a) it is clear that this ECD gives rise to a very local perturbation of the  
266 fringe field, in particular in the x-direction.

267 Figure 6(b) shows the corresponding components of  $B_x$ ,  $B_y$ , and  $B_z$  along the beam CAX with the presence of the  
268 heaviest ECD design. We note here that the  $B_x$  and  $B_y$  components at CAX without the ECD are very close to 0 T  
269 and so have been omitted for clarity. A maximum of 0.3 T transverse ( $B_x$ ) field is generated between the magnet banks  
270 which causes the deflection process. It is expected that with utilization of passive shimming full imaging potential  
271 should be restored for the 1 T MRI system as the impact of the ECD at the DSV is not negligible, but within shimming  
272 tolerances.

#### 273 **Mechanical and Design Performance**

274 The net force acting on the ECD was calculated to be between 151-1773 N and directed, due to obvious symmetry  
275 reasons, mostly towards the isocentre of the MRI-linac system. In the worst case scenario where say the ECD is directly  
276 above isocentre we need to sum the magnetic force to the weight of the ECD to get the total force. These forces are  
277 relatively small and easily managed from a design perspective as it is expected to be mounted by a heavy duty  
278 aluminium frame that surrounds the ECD. This frame will be integrated into the generic supporting frame housing  
279 the linac MLCs. Hence from a design and construction point of view the optimal ECD is viable.

280 There is one set of anomalies shown in figure 5 regarding the forces acting on the ECD. These are the three ECD  
281 models with the thinnest amount of steel and magnets ( $D = 4-8$  cm,  $T = 1$  cm,  $S = 0.5$  cm). As expected the non  
282 uniformity introduced is some of the lowest however the forces are some of the highest. Inspection of the flux maps  
283 revealed that these 3 ECD models were not able to utilize the steel frame for flux focusing. The magnets were too  
284 small to encourage significant flux to travel across the gap or around the steel frame, especially considering that they  
285 are in the stronger background MRI fringe field in the z-direction. As a result these ECD models generated only a  
286 small local perturbation to the MRI fringe field and so they were naturally strongly attracted towards the isocentre.  
287 In the next larger ECD designs ( $T = 2$  cm,  $S = 1$  cm) local flux changes were much stronger and the resultant forces  
288 dropped considerably. However from that point the force increases approximately proportional to the mass of the steel  
289 in the model.

## 290 Performance on purging electron contamination

291 In terms of purging the electron contamination, the ideal ECD would generate a magnetic field that has only a  
292  $B_x$  component, i.e. zero for the other components. This would mean that electrons traveling along the CAX in the  
293  $-z$  direction would undergo a force directed in the  $-y$  direction, as detailed by the Lorentz force. However in our case  
294 where the ECD fields are essentially superimposed onto the relatively strong MRI fringe field in the  $z$  direction, the  
295 resultant magnetic force acting between the ECD magnet banks is comprised of approximately equal amounts of  $B_x$   
296 and  $B_z$ , as seen in figure 6(b). Further to this the  $B_x$  and  $B_z$  forces are very different from each other above and below  
297 the central ECD level, and almost no electrons have only a  $z$ -component as they travel towards the ECD. Thus we  
298 can expect the electrons to be deflected in a much more complicated manner than just a simple  $-y$  direction force.  
299 Preliminary modeling confirmed this via visualisation studies and so an immediate observation was that the majority  
300 of the higher energy electrons were purged into the  $-x$  side ECD magnet bank. It was evident then that these may be  
301 back-scattered, and return back to a similar origin, or conversely return to the beam path near CAX and continue to  
302 travel towards the phantom surface. In an effort to absorb these purged electrons rather than back-scatter them, the  
303 role of the HDPE magnet and steel covers was created. The ideal properties of this layer are (a) be non-magnetic,  
304 (b) be as thin as possible to allow the magnet banks to be as close to a  $20 \times 20 \text{ cm}^2$  field edge as possible, and (c) be  
305 made from a material which discourages back-scattering. The choice of 5 mm of HDPE for this role is a first estimate.  
306 There is scope for altering this material and thickness however is not the focus of the current work.

307 In the simplest case the performance of the ECD is determined by its ability to purge linac head generated electron  
308 contamination as it passes through the ECD. Screen captures of the Geant4 simulations showing just the electron  
309 paths, along with examination of the energy deposition along the beam CAX is a useful method to observe this effect  
310 as shown in Figure 7. Fig 7(a) shows the electron paths in the case of no magnetic field ( $B = 0 \text{ T}$ ), fig 7(b) shows the  
311 MRI field ( $B = \text{MRI}$ ), fig 7(c) shows the MRI field with inclusion of an optimal ECD, and fig 7(d) shows the MRI  
312 field with the same ECD and the helium region. The field size in each of these images is  $20 \times 20 \text{ cm}^2$  and the SID is  
313 160 cm.

314 It is immediately obvious in 7(b) how the MRI field acts to collect and focus the electron contamination. In 7(c)  
315 there is purging of contamination by the ECD however also the reintroduction of air-generated contamination particles.  
316 Finally in 7(d) the inclusion of the helium gas region minimizes air-generated contamination.

317 For a quantitative analysis figures 8, 9 and 10 show a summary of the key Monte Carlo simulation results for  $5 \times 5$   
318  $\text{cm}^2$ ,  $10 \times 10 \text{ cm}^2$  and  $20 \times 20 \text{ cm}^2$  beams with various ECDs. In each of these figures the top row shows the energy  
319 deposition per primary history (MeV/PH) along a central  $x$ - $z$  plane with magnetic flux lines superimposed, the middle  
320 row shows the corresponding 2D skin dose map at  $70 \mu\text{m}$  depth, and in the bottom row the corresponding  $x/y$  profiles  
321 at  $70 \mu\text{m}$  depth are compared with an average  $x/y$  profile at 15 mm depth. Part (a) is the zero magnetic field case  
322 while part (b) is with the MRI field. Part (c) shows the lightest ECD design without the helium zone. The properties  
323 of the particular ECD modeled are noted in the top figure. Part (d) shows the most massive ECD without the helium  
324 region while part (e) includes the helium region for this ECD.

325 The impact of an inefficient ECD is evident in parts (c) of each figure. There is simply not enough deflection  
326 occurring and the focused beam of electron contamination particles are allowed to pass through the ECD and still  
327 generate significant skin dose hot spots, however slightly shifted away from the beam CAX.

328 For the most efficient ECD designs (part d) the assumption made is that all above ECD contamination is purged  
329 from the beam and that the resultant skin dose increases are primarily from a combination of (1) a flat fluence of  
330 direct x-ray beam induced dose, (2) a pyramid shaped fluence of air-generated electrons below the ECD, and (3) a  
331 complicated fluence of electrons which scattered off the ECD magnet bank faces and returned to the beam traveling



332 towards the isocentre. This is mostly confirmed in part (e) where the helium gas region is included. The 2D skin  
333 dose maps and profiles describe the final resultant hot spots as a combination of the base x-ray beam produced flat  
334 dose profile (compare with part a), a pyramid shaped and significant layer induced by the air-generated electrons, and  
335 a complex hot spot of smaller contribution which arises from any rescattered electrons from the ECD magnet bank  
336 faces. We should also note that there is some contribution as well from the upper and lower helium gas region windows  
337 which act as a source of electron scatter.

338 In the simplest terms the only means for further reductions in skin dose would be to reduce the thickness of the  
339 helium gas region windows and to complete a study dedicated to optimising the actual shape and surface properties  
340 of the ECD magnet banks and steel structure so that rescattering is minimized. Such a study is outside the scope of  
341 the current work.

342 In summary there were 35 designs which gave almost identical and lowest skin dose hot spot increases for 5x5  
343 cm<sup>2</sup>. However at 10x10 cm<sup>2</sup> only 23 models achieved complete purging, and for 20x20 cm<sup>2</sup> this was 14 designs. The  
344 reduction in efficiency for the larger field sizes is related to there being an increase in the amount of re-scattered  
345 electrons for the larger x-ray field sizes as compared to the 5x5 cm<sup>2</sup> case. This is because the x-ray beam passes  
346 closer by the ECD magnet bank faces for the larger field sizes, and hence there is a greater probability that scattered  
347 electrons will travel to the banks and back again.

#### 348 IV. CONCLUSION

349 In this work we have modeled a prototype open bore 1 T inline MRI-linac system and have accurately matched the  
350 manufacturer's specifications on the characteristics of the MRI field. The accurate magnetic field map was used inside  
351 Geant4 Monte Carlo simulations to investigate our previous estimates on the expected high entry skin doses. For this  
352 system skin dose hotspots ranging from 230% of  $D_{\max}$  for a 5x5 cm<sup>2</sup> to 1400% of  $D_{\max}$  for a 20x20 cm<sup>2</sup> should be  
353 expected as the MRI field acts to collect and focus electron contamination as it travels towards the treatment volume.  
354 It should be noted that this result is unique to our 160 cm SID open bore design and so is not representative of lower  
355 field strength systems or smaller bore sizes.

356 In response to this issue a permanent magnet style electron contamination deflector or ECD has been modeled  
357 for its performance in purging the contamination. Various ECD designs were highly efficient at purging the electron  
358 contamination from the x-ray beam however this does not eliminate the reproduction of electrons in the extended  
359 air-column of the prototype MRI-linac system, as well as some backscatter from the ECD itself. To address the former  
360 issue, a large and practical portion of the air column has been modeled as helium gas encased in a 50  $\mu\text{m}$  thick HPDE  
361 bag. Monte Carlo simulations of this arrangement predict that purging of the contamination coupled with replacement  
362 of the air-column will act together to minimize the skin dose increases. The end result is a prediction that the 70  $\mu\text{m}$   
363 skin doses will moderately increase in a small hot-spot for the jaw defined field sizes of 5x5, 10x10 and 20x20 cm<sup>2</sup> to  
364 levels of 40%, 55% and 65% of  $D_{\max}$ . Surface doses of this magnitude represent small increases and as such should  
365 be practical in terms of expected patient skin dose response. The ECD is predicted to be a useful element of our 1 T  
366 prototype MRI-linac system.

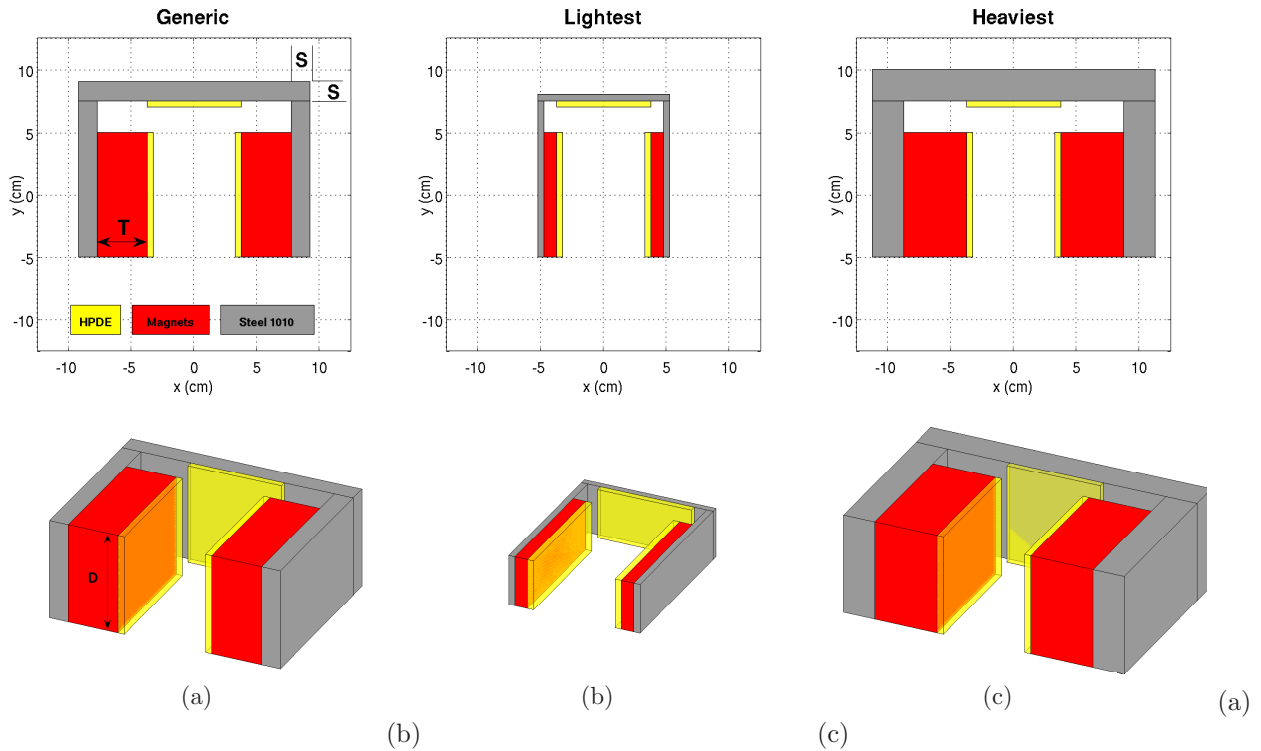


Figure 1: Schematic diagram of the electron contamination deflector (ECD). (a) Generic design showing the dimensions which were modeled heuristically: magnet thickness ( $T$ ), steel thickness ( $S$ ), magnet and steel depth ( $D$ ). (b) The least massive ECD modeled; 0.64 kg of NdFeB and 0.736 kg of steel 1010 (c) The most massive ECD modeled; 6.4 kg of NdFeB and 5.44 kg of steel 1010. Each design has a 5 mm thick high density polyethylene (HDPE) cover on the magnet surfaces facing the CAX as well as a portion of the steel circuit. The HDPE cover is designed to minimize deflected electrons scattering back in the x-ray beam.

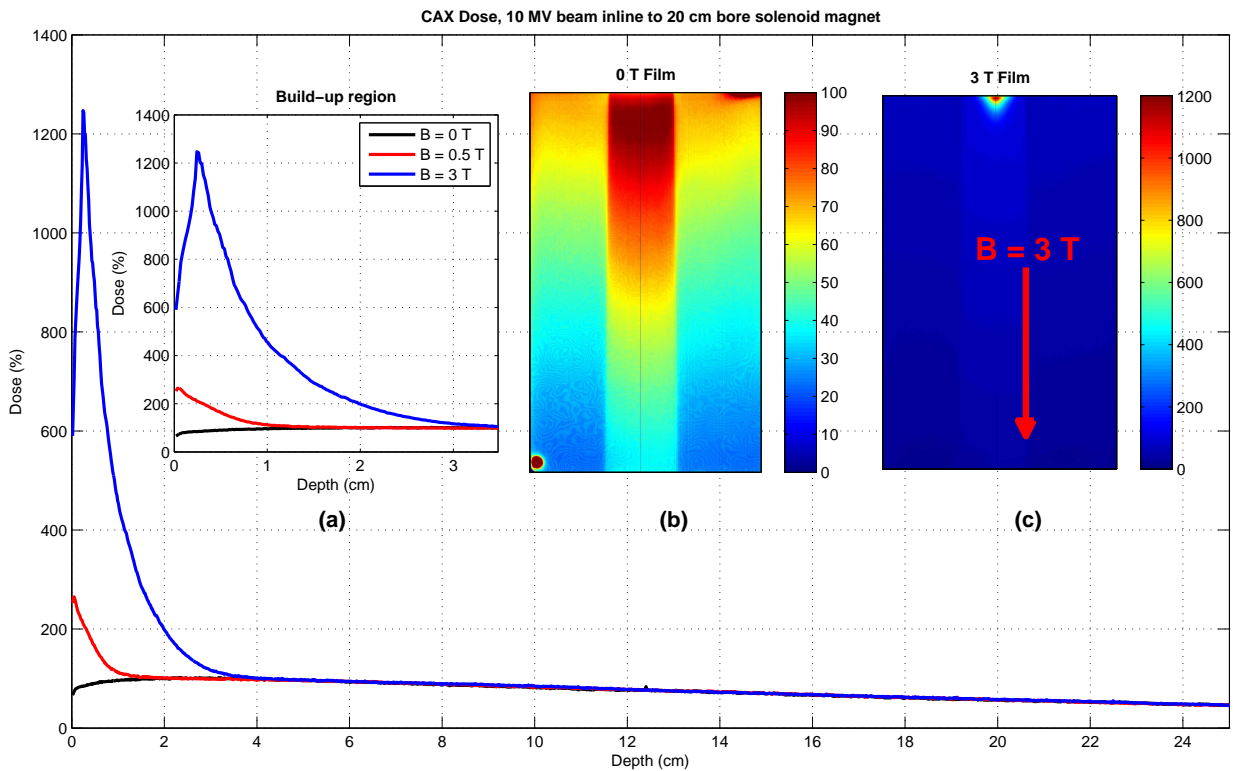


Figure 2: Experimental evidence of an inline magnetic fringe field acting to increase surface dose. Data presented here is reprocessed films from the 2001 experimental work by Litzenberg et al[10]. The main plot shows the central axis dose delivered by a 10 MV beam to a 20 cm diameter water phantom while exposed to 0 T, 0.5 T and 3 T inline magnetic fields. Insert part (a) shows a zoom of the build-up region while (b) and (c) show the 0 T and 3 T films that were exposed. The high surface doses seen at 0.5 T and 3 T are due to electron contamination being focused by the fringe field.

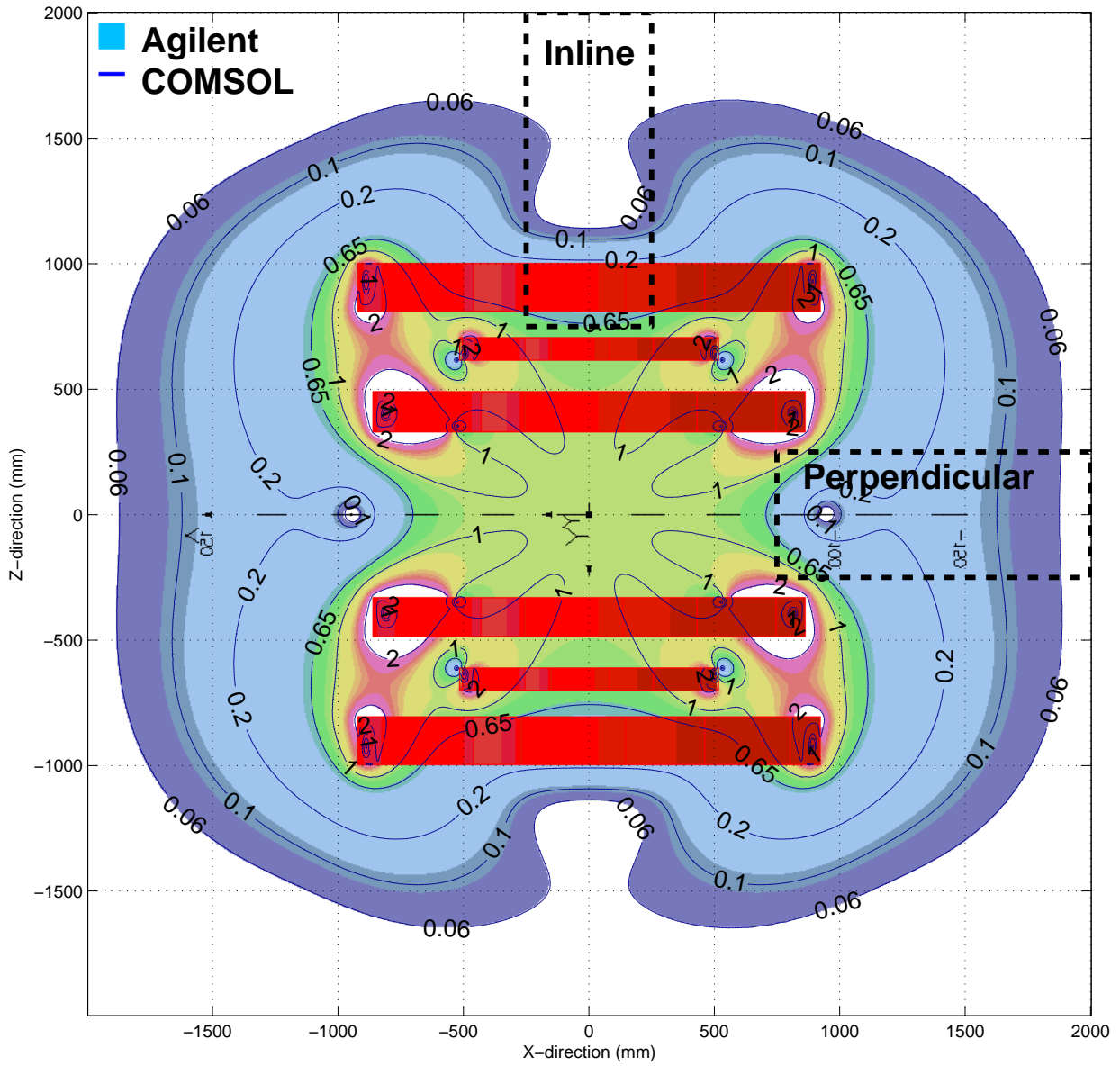


Figure 3: Magnetic field magnitude map of the Agilent 1 T MRI design (fill plot) and COMSOL (contour plot) match in the central x-z plane. Current coils are shown in red and below 0.06 T or above 2 T is shown as white. The agreement seen between our COMSOL results and the Agilent data is  $\pm 0.0001$  T inside the DSV. Also shown is the low magnetic field regions for positioning of the linac in either the perpendicular or inline orientation.

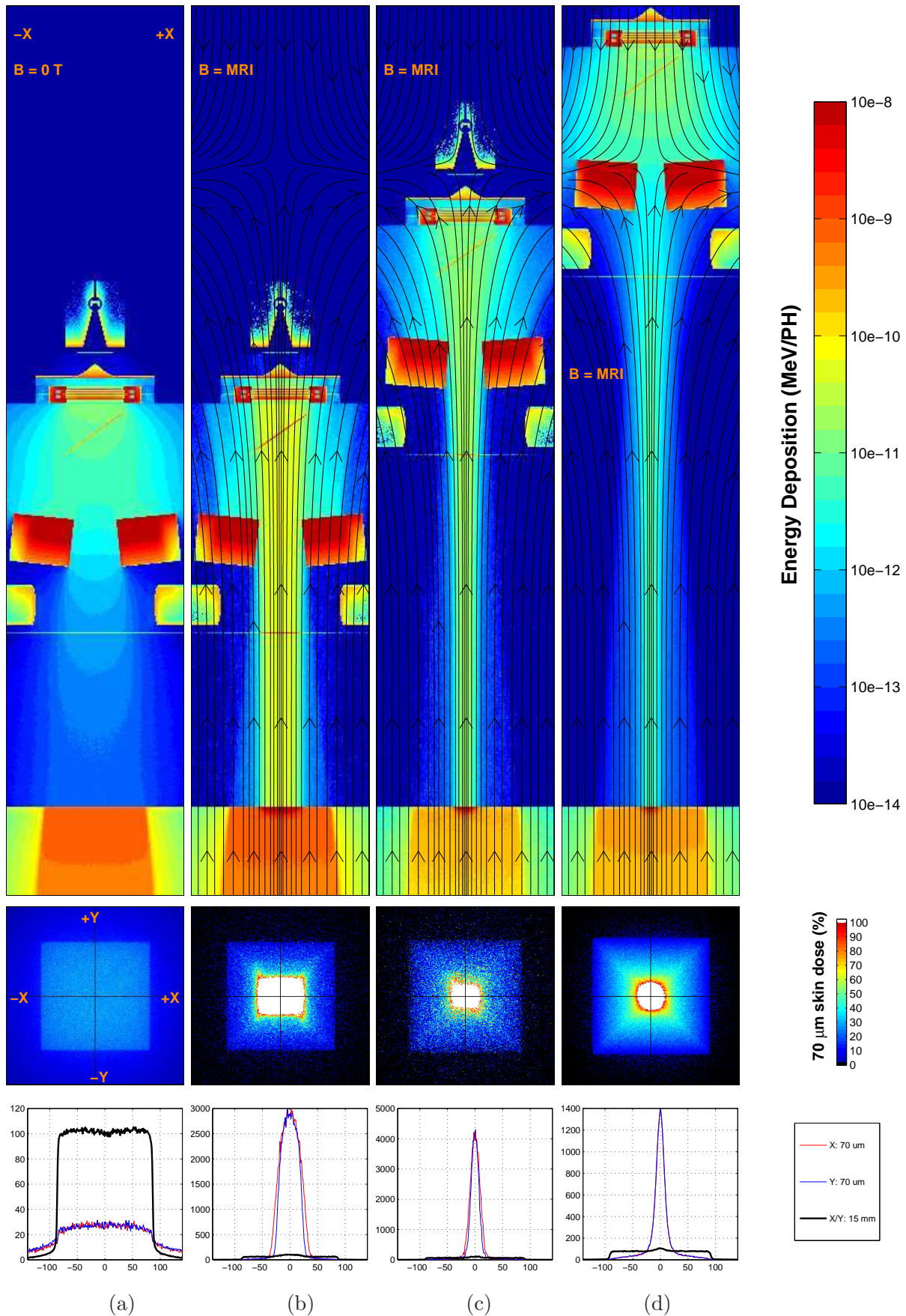


Figure 4: Energy deposition (top row), 2D skin dose (middle row) and skin dose x/y profiles vs Dmax profiles (bottom row) for a  $20\times 20\text{ cm}^2$  field. In (a) we see no magnetic field and an SID of 100 cm. (b) shows the MRI field and an SID of 100 cm. (c) shows the MRI field and an SID of 130 cm. (d) shows the MRI field and an SID of 160 cm. In the top row the energy deposition is on a log-scale to highlight the dose throughout the entire linac head, air column and phantom region. In the middle row the colormap is set to white at 100% dose or greater, and to black for  $< 2.5\%$  dose. The skin dose hot spots are due to the MRI field acting to force a high majority of electron contamination particles to travel towards the CAX and the phantom surface, particularly those generated from the base of the flattening filter and ion chamber.

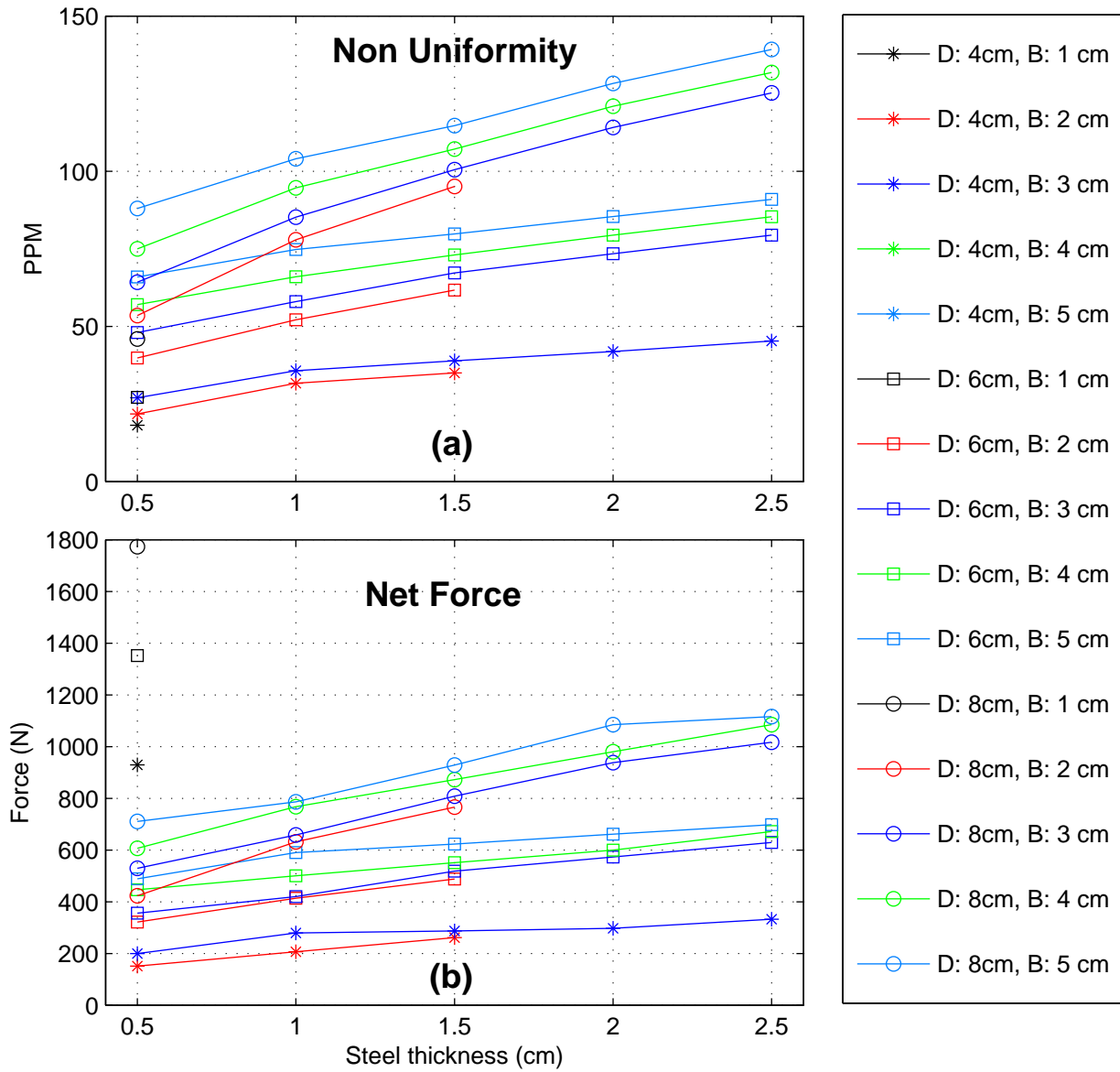


Figure 5: Impact on the MRI uniformity and net forces acting on the ECD. In (a) we see the non-uniformity introduced by the ECD models. All models are  $<300$  ppm and so will be correctable via active/passive shimming. In (b) we see the net force acting on the ECD. It is clear that increasing the overall mass of the ECD has a direct impact on the forces acting however these pose no engineering concerns. The anomaly seen with the forces acting on the 1 cm magnet thickness ( $T = 1$  cm,  $S = 0.5$  cm) models is attributed to the dominance of the MRI field over an inefficient magnetic circuit in the ECD.

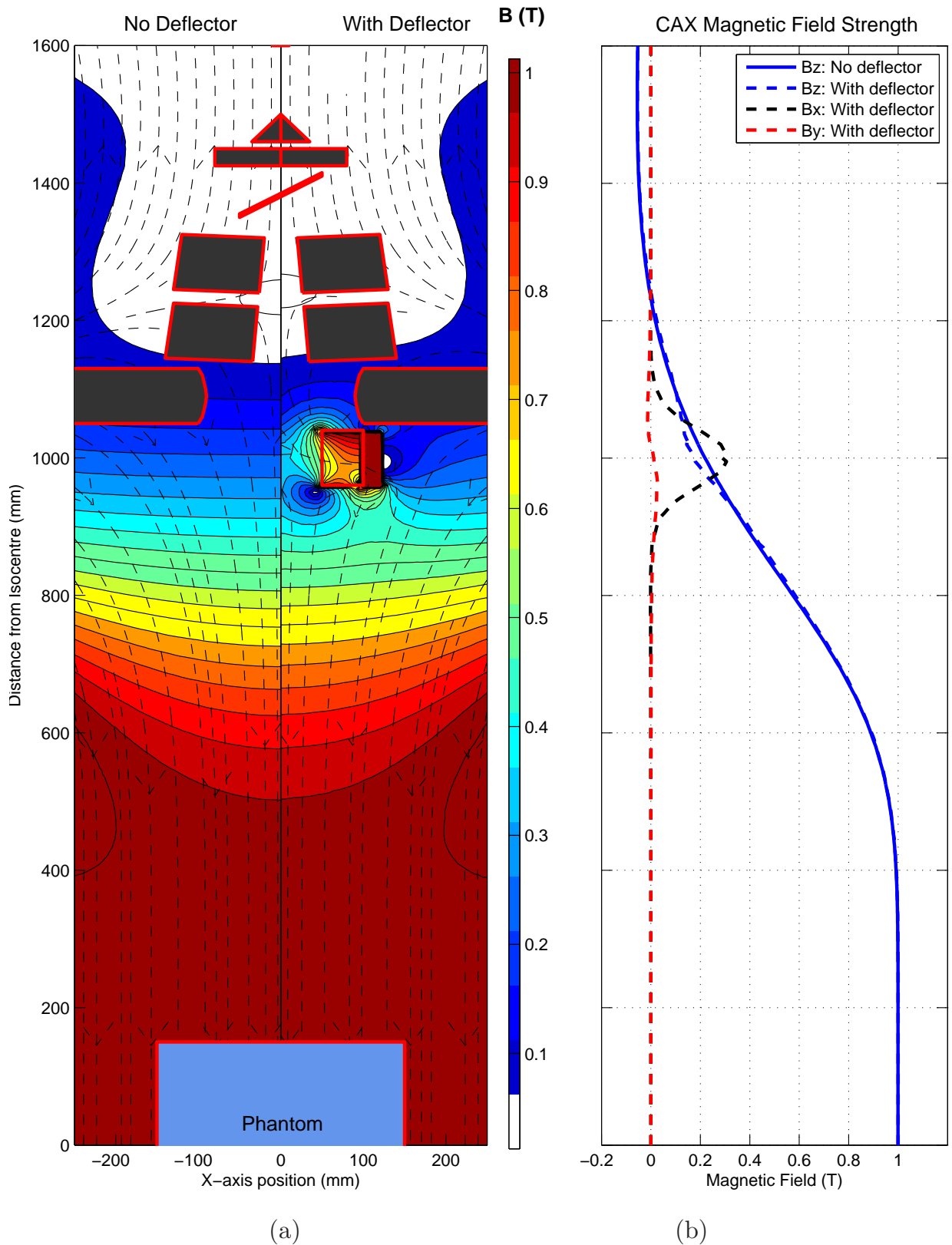


Figure 6: Magnetic field properties encompassing the linac (a) Left: No ECD, Right: With the heaviest ECD design present. Superimposed on these plots are Matlab (Natick, Massachusetts) streamslice plots of the magnetic field ( $B_z$ ) directions and linac components. In (b) plots of the magnetic field components along the CAX are shown. The ECD gives rise to a very localised  $B_x$  field which is used to purge the electron contamination.

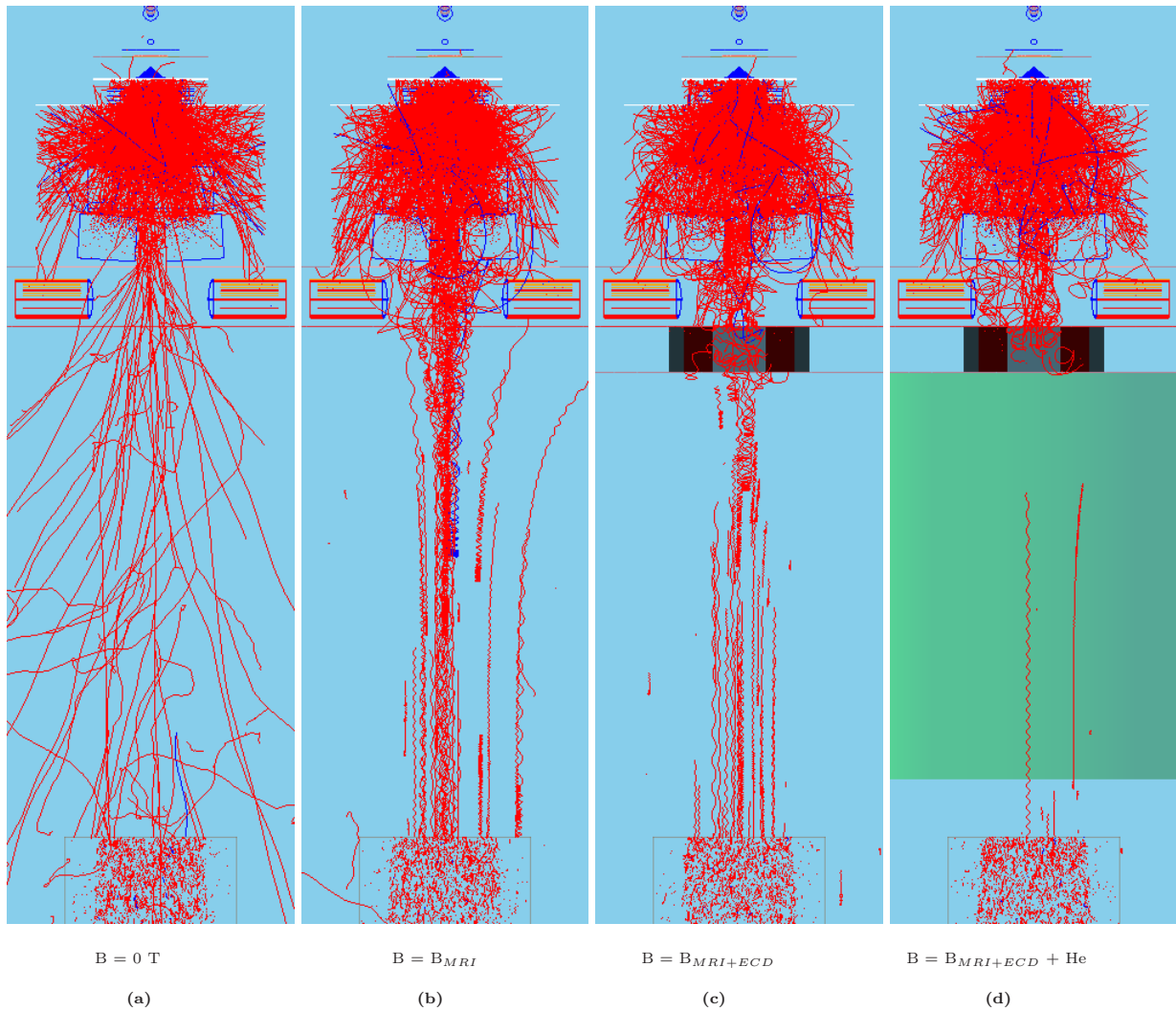


Figure 7: Demonstration of the skin dose hot spot reduction by using the ECD and helium region: the electron contamination paths. In each plot the SID = 160 cm, an x-ray field size of  $20 \times 20 \text{ cm}^2$  is shown, and 10,000 particles were fired from the phase space file at the base of flattening filter. (a)  $B = 0 \text{ T}$  (no magnetic field). (b)  $B = MRI$ , same as (a) except the MRI field is included. (c) Inclusion of an optimal ECD. (d) Inclusion of an optimal ECD and helium gas region below the ECD of 71.2 cm. It is clear from parts (c) and (d) that in order to reduce the amount of electron contamination arriving at the phantom surface that a combination of both a ECD and helium gas region is required.

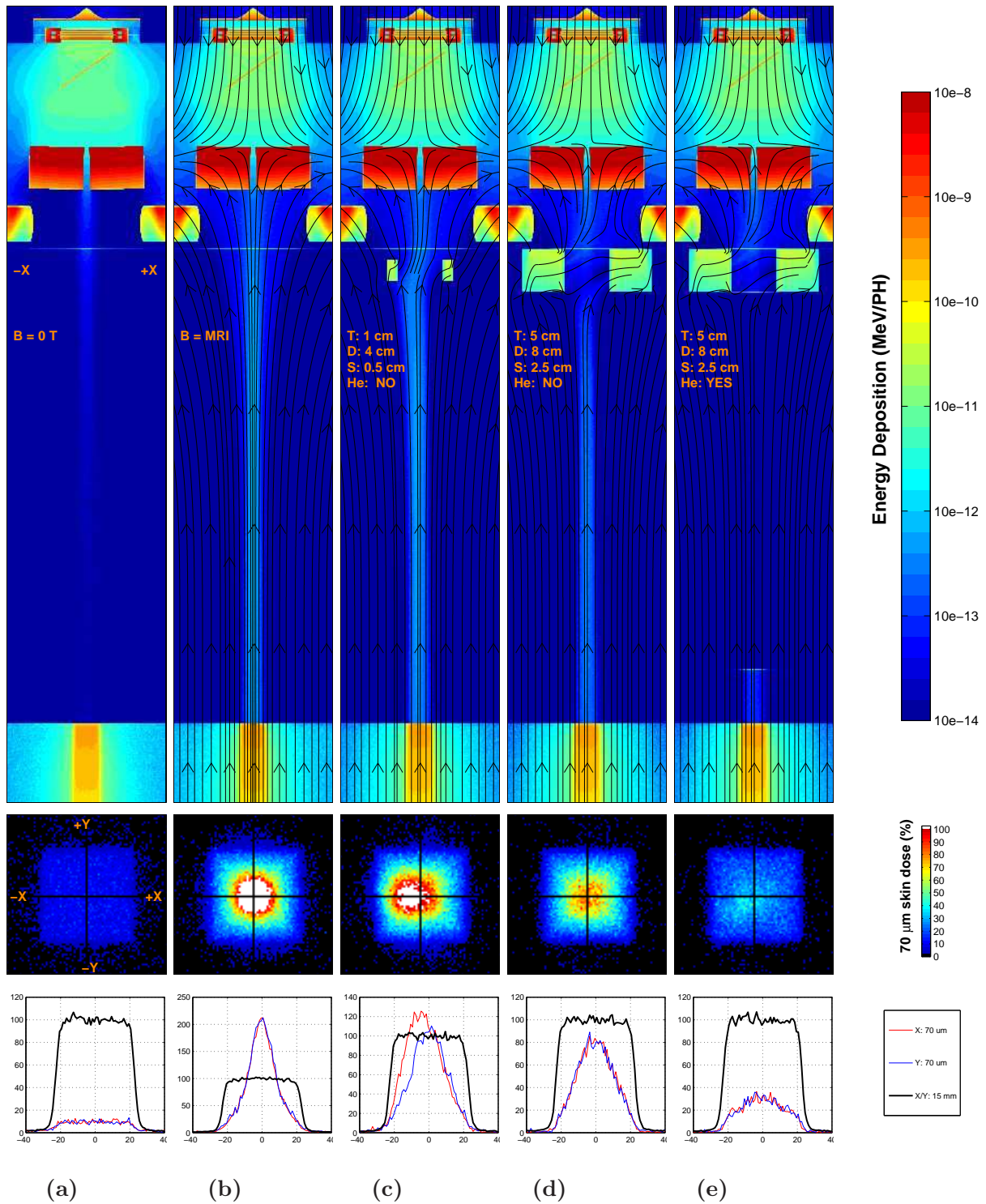


Figure 8: Energy deposition (top row), 2D skin dose (middle row) and skin dose x/y profiles vs  $D_{max}$  profiles (bottom row) for a  $5 \times 5 \text{ cm}^2$  field. In (a) we see no magnetic field. (b) shows the MRI field. (c) shows the smallest and inefficient ECD design where not all head generated contamination is purged. (d) shows the most efficient ECD with air below while (e) shows the most efficient ECD with the addition of the helium region. In the top row the energy deposition is on a log-scale to highlight the dose throughout the entire linac head, air column and phantom region. In the middle row the colormap is set to white at 100% dose or greater, and to black for  $< 2.5\%$  dose.



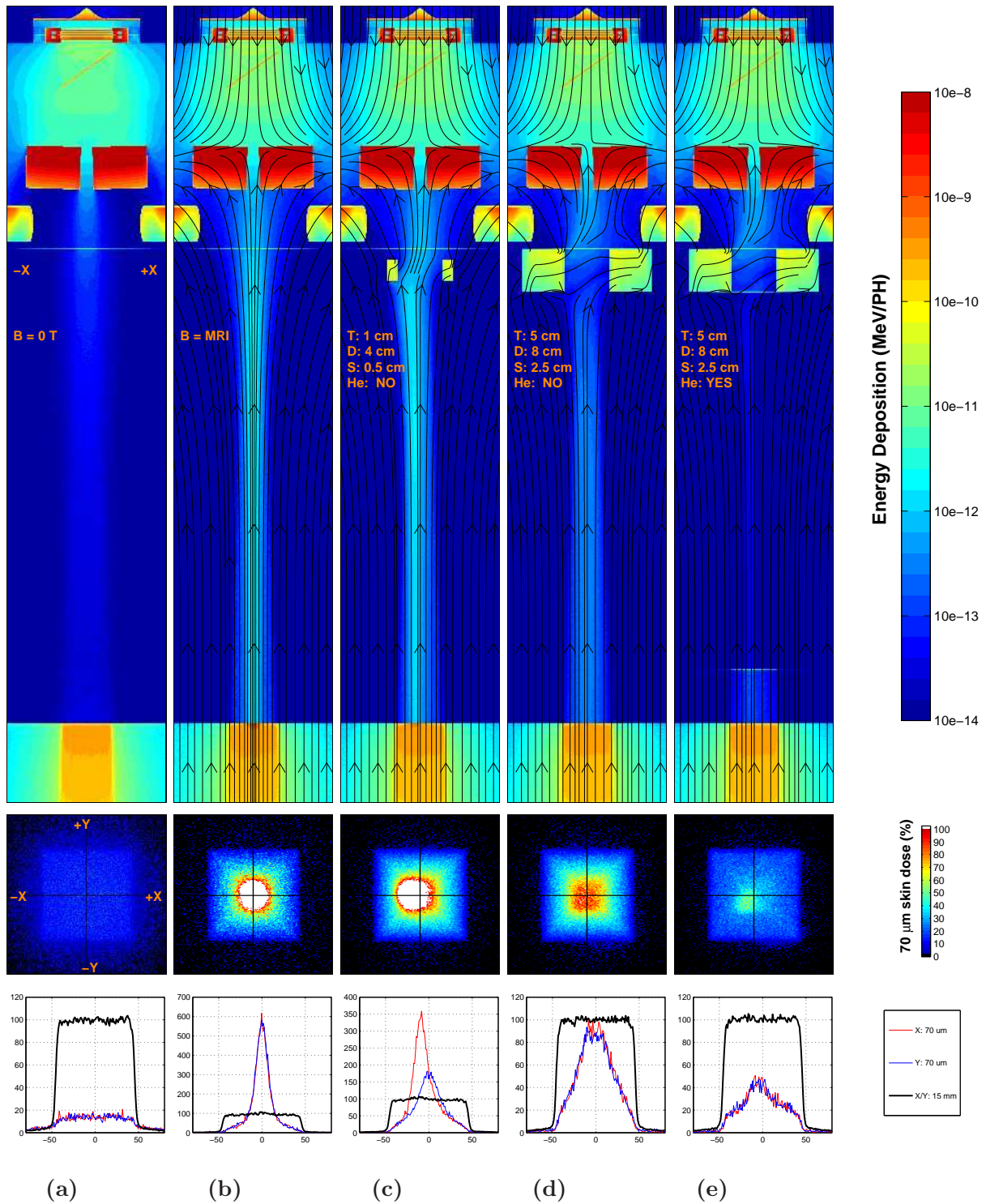


Figure 9: Energy deposition (top row), 2D skin dose (middle row) and skin dose x/y profiles vs  $D_{\text{max}}$  profiles (bottom row) for a  $10 \times 10 \text{ cm}^2$  field. In (a) we see no magnetic field. (b) shows the MRI field. (c) shows the smallest and inefficient ECD design where not all head generated contamination is purged. (d) shows the most efficient ECD with air below while (e) shows the most efficient ECD with the addition of the helium region. In the top row the energy deposition is on a log-scale to highlight the dose throughout the entire linac head, air column and phantom region. In the middle row the colormap is set to white at 100% dose or greater, and to black for  $< 2.5\%$  dose.

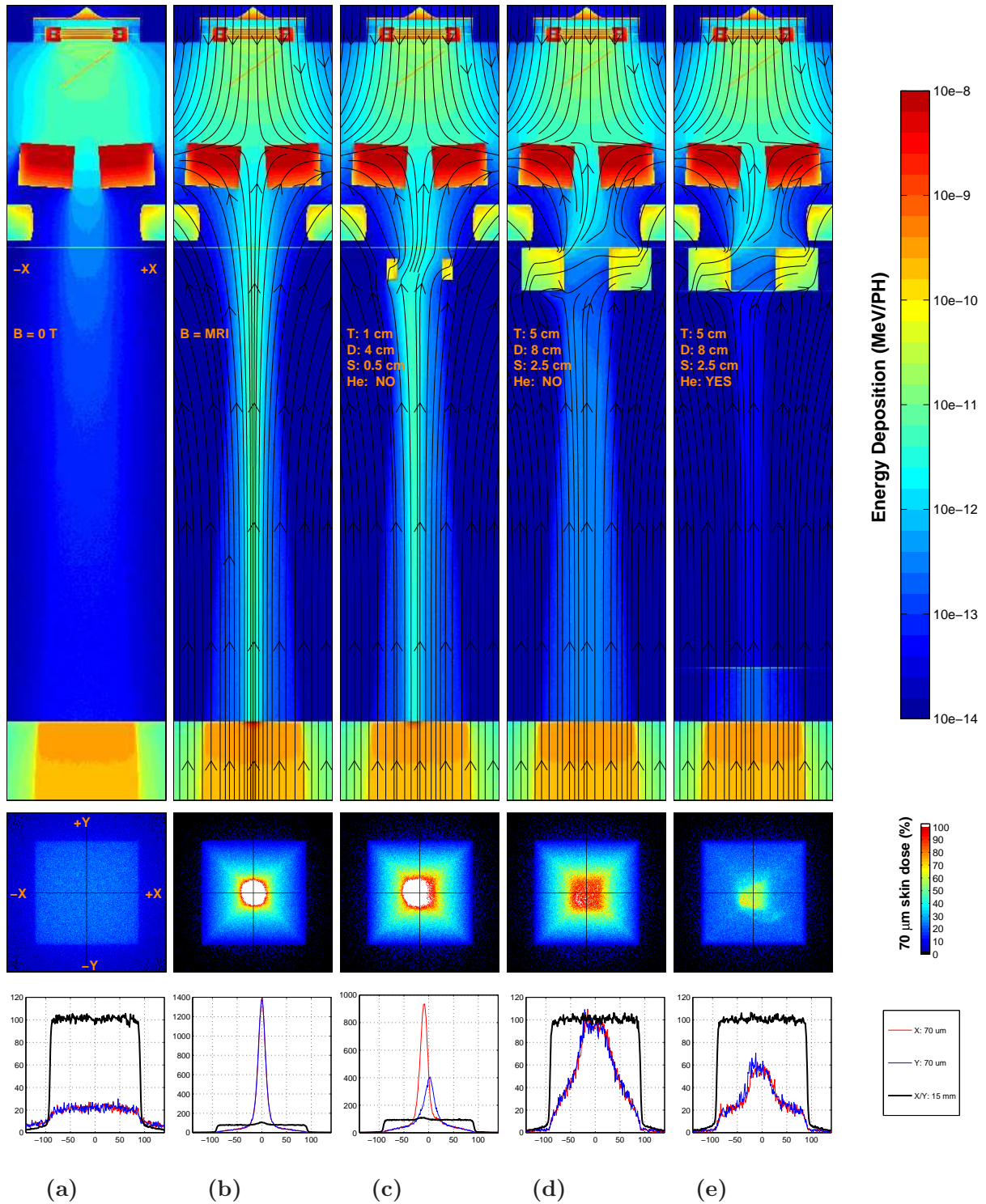


Figure 10: Energy deposition (top row), 2D skin dose (middle row) and skin dose x/y profiles vs  $D_{\max}$  profiles (bottom row) for a  $20 \times 20 \text{ cm}^2$  field. In (a) we see no magnetic field. (b) shows the MRI field. (c) shows the smallest and inefficient ECD design where not all head generated contamination is purged. (d) shows the most efficient ECD with air below while (e) shows the most efficient ECD with the addition of the helium region. In the top row the energy deposition is on a log-scale to highlight the dose throughout the entire linac head, air column and phantom region. In the middle row the colormap is set to white at 100% dose or greater, and to black for  $< 2.5\%$  dose.

## References

- 367
- 368 [1] B W Raaymakers, J J W Lagendijk, J Overweg, J G M Kok, A J E Raaijmakers, E M Kerkhof, R W van der Put,  
369 I Meijnsing, S P M Crijns, F Benedosso, M van Vulpen, C H W de Graaff, J Allen, and K J Brown. Integrating a 1.5 T  
370 MRI scanner with a 6 MV accelerator: proof of concept. *Phys. Med. Biol.*, 54:N229–N237, 2009.
- 371 [2] BG Fallone, B. Murray, S. Rathee, T. Stanescu, S. Steciw, S. Vidakovic, E. Blosser, and D. Tymofichuk. First mr images  
372 obtained during megavoltage photon irradiation from a prototype integrated linac-mr system. *Medical physics*, 36:2084,  
373 2009.
- 374 [3] J.F. Dempsey, D. Benoit, J.R. Fitzsimmons, A. Haghghat, J.G. Li, D.A. Low, S. Mutic, J.R. Palta, H.E. Romeijn, and  
375 G.E. Sjoden. A device for realtime 3D image-guided IMRT. *I. J. Radiation Oncology, Biology/Physics*, 63 (2):S202, 2005.
- 376 [4] Drago E. Constantin, Rebecca Fahrig, and Paul J. Keall. A study of the effect of in-line and perpendicular magnetic fields  
377 on beam characteristics of electron guns in medical linear accelerators. *Medical Physics*, 38(7):4174–4185, 2011.
- 378 [5] B. M. Oborn, P. E. Metcalfe, M. J. Butson, and A. B. Rosenfeld. High resolution entry and exit Monte Carlo dose  
379 calculations from a linear accelerator 6 MV beam under influence of transverse magnetic fields. *Med. Phys.*, 36(8):3549–  
380 3559, 2009.
- 381 [6] B. M. Oborn, P. E. Metcalfe, M. J. Butson, and A. B. Rosenfeld. Monte Carlo characterization of skin doses in 6 mv  
382 transverse field mri-linac systems: Effect of field size, surface orientation, magnetic field strength, and exit bolus. *Medical  
383 Physics*, 37(10):5208–5217, 2010.
- 384 [7] BM Oborn, PE Metcalfe, MJ Butson, AB Rosenfeld, and PJ Keall. Electron contamination modeling and skin dose in 6  
385 mv longitudinal field mrigrt: Impact of the mri and mri fringe field. *Medical physics*, 39(2):874, 2012.
- 386 [8] A Keyvanloo, B Burke, B Warkentin, T Tadic, S Rathee, C Kirkby, D. M Santos, and B. G. Fallone. Skin dose in  
387 longitudinal and transverse linac-MRIs using Monte Carlo and realistic 3D MRI models. *Med. Phys.*, 39(10):6509–6521,  
388 2012.
- 389 [9] Tristan C F van Heijst, Mariska D den Hartogh, Jan J W Lagendijk, H J G Desire van den Bongard, and Bram van  
390 Asselen. Mr-guided breast radiotherapy: feasibility and magnetic-field impact on skin dose. *Physics in Medicine and  
391 Biology*, 58(17):5917, 2013.
- 392 [10] D. W. Litzenberg, B. A. Fraass, D. L. McShan, T. W. ODonnel, D. A. Roberts, F. D. Becchetti, A. F. Bielajew, and J. M.  
393 Moran. An apparatus for applying strong longitudinal magnetic fields to clinical photon and electron beams. *Phys. Med.  
394 Biol.*, 46:N105115, 2001.
- 395 [11] Yu Chen, Alex F. Bielajew, Dale W. Litzenberg, Jean M. Moran, and Frederick D. Becchetti. Magnetic confinement of  
396 electron and photon radiotherapy dose: A monte carlo simulation with a nonuniform longitudinal magnetic field. *Medical  
397 Physics*, 32(12):3810–3818, 2005.
- 398 [12] B. Nilsson and A. Brahme. Absorbed dose from secondary electrons in high energy photon beams. *Phys. Med. Biol.*,  
399 24:901–912, 1979.
- 400 [13] P. D. LaRiviere. Surface dose from 6MV photon interactions in air. *Phys. Med. Biol.*, 28:285–287, 1983.
- 401 [14] E. D. Yorke, C. C. Ling, and S. Rustgi. Air-generated electron contamination of 4 and 10MV photon beams: a comparison  
402 of theory and experiment. *Phys. Med. Biol.*, 30:1305–1314, 1985.
- 403 [15] R. Sjogren and M. Karlsson. Electron contamination in high energy photon beams. *Med. Phys.*, 23(11):1873–1881, 1996.
- 404 [16] M. J. Butson, P. K. N. Yu, and P. E. Metcalfe. Incident contamination lepton doses measured using radiochromic film in  
405 radiotherapy. *Radiation Measurements*, 29:605–609, 1998.
- 406 [17] M. J. Butson, T. Cheung, P. Yu, and P. E. Metcalfe. Evaluation of a radiotherapy electron contamination defecting system.  
407 *Radiation Measurements*, 32:101–104, 2000.
- 408 [18] Antonio Lopez Medina, Antonio Teijeiro, Juan Garcia, Jorge Esperon, J. Antonio Terron, Diego P. Ruiz, and Maria C.  
409 Carrion. Characterization of electron contamination in megavoltage photon beams. *Med. Phys.*, 32(5):1281–1292, 2005.
- 410 [19] T. N. Padikal and J. A. Deye. Electron contamination of a high-energy x-ray beam. *Phys. Med. Biol.*, 23:1086–1092, 1978.
- 411 [20] P. J. Biggs and C. C. Ling. Electrons as the cause of the observed shift in dmax with field size in high energy photon  
412 beams. *Med. Phys*, 6:p291–295, 1979.
- 413 [21] C. C. Ling, M. C. Schell, and S. N. Rustgi. Magnetic analysis of the radiation components of a 10MV photon beam. *Med.  
414 Phys.*, 9:20–26, 1982.
- 415 [22] P. J. Biggs and M. D. Russell. An investigation in the presents of secondary electrons in megavoltage photon beams. *Phys.  
416 Med. Biol.*, 28:1033–1043, 1983.
- 417 [23] G. Krithivas and S. N. Rao. A study of the characteristics of radiation contaminants within a clinically useful photon beam.  
418 *Med. Phys.*, 12:764–768, 1985.

- 419 [24] B. R. Thomadsen, S. S. Kubsad, B. R. Paliwal, S. Shahabi, and T. R. Mackie. On the cause of the variation in tissue-  
420 maximum ratio values with source-to-detector distance. *Med. Phys.*, 20(3):723–727, 1993.
- 421 [25] D. M. D. Frye, B. R. Paliwal, B. R. Thomadsen, and P. Jursinic. Intercomparison of normalized head-scatter factor  
422 measurement techniques. *Med. Phys.*, 22(2):249–253, 1995.
- 423 [26] P. A. Jursinic and T. R. Mackie. Characteristics of secondary electrons produced by 6, 10 and 24 MV x-ray beams. *Phys.*  
424 *Med. Biol.*, 41:1499–1509, 1996.
- 425 [27] M. J. Butson, T. P. Y. Wong, A. Law, M. Law, J. N. Mathur, and P. E. Metcalfe. Magnetic replusion of linear accelerator  
426 contaminants. *Med. Phys.*, 23 (6):953–955, 1996.
- 427 [28] R. Sjogren and M. Karlsson. Inuence of electron contamination on in vivo surface dosimetry for high-energy photon beams.  
428 *Med. Phys.*, 25(6):916–921, 1998.
- 429 [29] COMSOL multiphysics. Stockholm, Sweden.
- 430 [30] Stefan Kolling, Brad Oborn, and Paul Keall. Impact of the mlc on the mri field distortion of a prototype mri-linac. *Medical*  
431 *Physics*, 40(12):–, 2013.
- 432 [31] S. Agostinelli et al. Geant4-a simulation toolkit. *Nucl. Instrum. Methods Phys. Res. A*, 506:250–303, 2003.
- 433 [32] A. J. E. Raaijmakers, B. W. Raaymakers, and J. J. W. Lagendijk. Experimental verification of magnetic field dose effects  
434 for the MRI-accelerator. *Phys. Med. Biol.*, 52:4283–4291, 2007.
- 435 [33] Varian Medical Systems. Palo Alto, CA.
- 436 [34] International Commission on Radiological Protection. ICRP Publication 59, The Biological Basis for Dose Limitation in  
437 the Skin. *Annals of the ICRP*, 22(2), 1992.
- 438 [35] Liu F Crozier S. Liu L, Sanchez-Lopez H. Flanged-edge transverse gradient coil design for a hybrid LINAC-MRI system.  
439 *J Magn Reson.*, 226:70–8, 2013.